Carbon 244 (2025) 120705

Contents lists available at ScienceDirect

Carbon

journal homepage: www.elsevier.com/locate/carbon

# Trimesic acid-derived Cu embedded in carbon nano-octahedrons for electrocatalytic quantification of trace metformin in water matrices

Yu-Jen Shih [a,*], Zhi-Lun Wu [a], Wei-Hsiang Chen [a], Yu-Hsuan Liu [a], Chin-Pao Huang [b]

[a] Institute of Environmental Engineering, National Sun Yat-sen University, Taiwan
[b] Department of Civil and Environmental Engineering, University of Delaware, Newark, 19716, DE, USA

ARTICLE INFO

*Keywords:*
Pharmaceutical
Biguanide
Metal organic frameworks
Nano-octahedron
Surface complexation

ABSTRACT

The widespread use of anti-diabetic pharmaceuticals has become a significant environmental concern. This study reports the synthesis of a trimesic acid framework, CuBTC/PVP, comprising benzene-1,3,5-tricarboxylic acid and polyvinylpyrrolidone, and its pyrolyzed copper-carbon materials for electrochemical detection of metformin (MTF). Upon carbonization, the resulting composite, featuring copper nanoparticles (NPs) and nanoclusters embedded in carbon nano-octahedrons (CuCNO), substantially improved the effective surface area and charge transfer efficiency for sensoring applications. Redox transitions between Cu(I) and Cu(II) on Cu sites mediated the oxidation of surface-chelated biguanide Cu(II)-MTF complexes, as supported by electron density calculations. Pyrolysis temperature controlled crystallite size and dispersity of Cu NPs in CNO, so to optimize the voltammetric current density at approximately +1.0 V (vs. RHE) for CuCNO(400). The pH-dependent peak potential shifts and free energy calculations revealed that the double chelation of MTF at high pH greatly enhanced detection sensitivity. The electrode demonstrated excellent reproducibility, selectivity, and analytical recovery in real water samples, including river, lake, and wastewater effluent. It achieved a highly linear anodic current across MTF concentrations of 0.5–50 μg $L^{-1}$, with a detection limit of 0.054 μg $L^{-1}$.

## 1. Introduction

Pharmaceuticals represents a major subgroup of emerging pollutants, contaminating the environment through their manufacture, use, and disposal [1]. Substances such as antibiotics, analgesics, and non-steroidal anti-inflammatory drugs (NSAIDs) are found in hospital and municipal wastewaters, with concentrations ranging from ng $L^{-1}$ to mg $L^{-1}$ – levels that rise markedly in recent years, particularly during the pandemic [2]. Many of these pharmaceuticals are persistent, bio-accumulative, and pose ecological risks to aquatic organisms. Active pharmaceutical ingredients (APIs), including carbamazepine, caffeine, and metformin, resist to complete mineralization in conventional wastewater treatment plants (WWTPs) [3]. Moreover, the formation of chlorinated byproducts during disinfection processes further exacerbates environmental concerns. To address these challenges, effective methods are needed to monitor a diversity of pharmaceutical pollutants. Although laboratory-scale analytical techniques like gas chromatography (GC) and high-performance liquid chromatography (HPLC) provide accurate trace-level detection for pharmaceutical pollutants, they are expensive, non-portable, and less suitable for routine field monitoring [4]. Electrochemical devices offer a straightforward and user-friendly alternative, enabling selective quantification in complex water matrices due to the distinct redox potentials of various contaminants [5]. In this study, metformin (MTF, N,N-dimethylbiguanide) is selected as a model pharmaceutical due to its widespread use in type-II diabetes treatment. Classified by the WHO as an essential medicine for managing hypoglycemia [6], MTF is among the most frequently found drugs in surface and wastewater. Despite being not a hormone mimic, MTF can still disrupt the endocrine systems of aquatic vertebrates, such as fish and mammals [7]. Particularly, its persistence and bio-accumulation in living organisms and the environment are associated with potential health risks, such as lactic acidosis or vitamin B12 deficiency [8]. Owing to its widespread use, MTF has been detected at adverse levels in various waste sources, ranging from 10 to 100 μg $L^{-1}$ in sewage treatment plant, 3–100 μg $L^{-1}$ in water reclamation facility, and approximately 10 μg $L^{-1}$ in river catchments [8].

The limited versatility of commercial electrodes such as glassy carbon (GCE) and carbon paste (CPE) in analyzing a broad range of pollutants stems from their lack of active metals. Previous studies have shown that MTF molecules specifically chelated with copper metal or

* Corresponding author.
*E-mail address:* yjshih@mail.nsysu.edu.tw (Y.-J. Shih).

https://doi.org/10.1016/j.carbon.2025.120705
Received 8 July 2025; Received in revised form 31 July 2025; Accepted 8 August 2025
Available online 9 August 2025

oxides, inducing intrinsic potential-current responses at their characteristic redox potentials [9]. MOF-derived materials enable the integration of metal species into carbon frameworks using organic linkers such as imidazolate (ZIF), benzene-1,3,5-tricarboxylates (BTC), and benzene-1,4-dicarboxylic acid (BDC), thereby enhancing the electrochemical surface area (ECSA) and redox sensitivity toward target analytes [10]. BTCs – known as trimesic acid – feature alternating tetrahedral or octahedral coordination geometries. This structural versatility has led to wide exploration in applications such as gas separation, catalysis, and biomedical engineering [11]. Their physicochemical properties can be tailored by varying the coordinated metal ions, such as $Cu^{2+}$, $Fe^{2+}$, $Mn^{2+}$, and $Co^{2+}$ [12,13]. CuBTC, in particular, presents a compelling alternative to traditional Cu deposition on carbon supports, as it allows for the atomic-scale dispersion of Cu sites within a stable carbon framework.

Electrochemically sensing of MTF is driven by the complexation and activation of $Cu^{2+}$-biguanide species [14,15]. The redox transition of $Cu^{2+}$-to-$Cu^{+}$ in $Cu^{2+}$-MTF complexes adsorbed on electrode surfaces facilitates metal-to-ligand charge transfer, enabling MTF oxidation at specific anodic potentials [16]. While soluble copper salts such as $CuCl_2$ and $Cu(NO_3)_2$ are employed in homogeneous approaches, their use leads to waste generation and environmental concerns. To address the above limitation, copper metal or oxide nanoparticles (NPs) can be synthesized as active sites for MTF detection. The novelty of this study lies in the utilization of CuBTC, instead of conventional copper-carbon composites, as a precursor for the electro-sensor. CuBTC is deemed to enhance the redox reactivity and sensitivity of Cu sites toward MTF. The incorporation of polyvinylpyrrolidone (PVP) as a structure-directing modifier controlled the geometry and particle size of CuBTC/PVP during solvothermal synthesis [17,18]. Subsequent pyrolysis intercalated Cu crystallites or nanoclusters into the mesoporous carbon nano-octahedrons (CuCNO). Effects of carbonization degree on MTF sensing sensitivity and stability at trace quantities were evaluated. The redox mechanism, analytical recovery, selectivity against interfering species, and the limit of detection for MTF were investigated through voltammetry and chronoamperometry modes.

## 2. Experimental section

The methodology, including details on chemical regents, preparation procedures, characterization techniques, and measurement protocols, is provided in Supporting Information S1. CuBTC/PVP and the derived CuCNO(300–700) composites are synthesized via a solvothermal process, as shown in Scheme 1.

## 3. Results and discussion

### 3.1. Characterization

As shown in Fig. 1a, the synthesized CuBTC/PVP exhibits well-defined single crystals with an octahedral morphology. Compared to conventional Cu-BTC, commonly known as MOF-199 or HKUST-1 ($Cu_3BTC_2$) [19], the average grain size is greatly reduced from around 10 μm (inset of Fig. 1a) to 200–400 nm due to the templating effect of the PVP modifier [20]. Upon pyrolysis at 400 °C, $Cu^{2+}$ nodes migrate from the organic framework and nucleate into nanoparticles (NPs) embedded within the carbon polyhedrons (Fig. 1b). Meanwhile, the CuBTC/PVP structure undergoes moderate shrinkage when BTC linkers are gradually carbonized into an inorganic carbon nano-octahedron (CNO). At higher temperatures (700 °C, Fig. 1c), the Cu NPs coarsen into clusters anchored along the CNO edges due to the Ostwald ripening effect [21]. Notably, elemental analysis reveals an increased atomic percentage of oxygen around Cu sites, suggesting the recrystallization of metal oxide in the clusters. High-magnification TEM images reveal that the porous CNO framework effectively encapsulates Cu clusters (Fig. 1d), which are composed of rod-like crystallites with an average diameter of 10 nm (Fig. 1e), indicating their polycrystalline nature. The selected-area electron diffraction (SAED) in Fig. 1f, acquired from the Cu particles, displays distinct concentric rings, corresponding to mixed diffraction patterns of $Cu_2O$ and CuO phases [22]. The HRTEM image shows a lattice d-spacing of 0.246 nm, indexed to the (1 1 1) plane for Cu oxides [23]. Elemental mappings of CuBTC/PVP and CuCNO(400) are shown in Fig. 1g and h, respectively. Uniform distribution of C, N, O, and Cu signals in CuBTC/PVP suggests a long-range ordered metal-organic crystallinity. After carbonization, the porous carbon skeleton in CuCNO is particularly assembled by C and N elements, while O is concentrated around the embedded clusters in CNO matrix, indicating the oxidation of copper.

The crystal structures of pyrolyzed CuCNO are characterized via XRD, as shown in Fig. 2a. The major diffraction peaks of the CuBTC/PVP precursor appear at 2θ of 6.9°, 9.4°, 11.5°, 13.6°, and 19.1°, corresponding to (2 0 0), (2 2 0), (2 2 2), (4 0 0), and (4 4 0) planes, respectively, verifying the formation of standard HKUST-1 (Cambridge Structural Database 112954) [24]. Upon heating to 300 °C, metallic copper (Fm $\bar{3}$ m(225)) emerges, with (1 1 1), (2 0 0), and (2 2 0) planes at 2θ of 43.3°, 50.4°, and 74.1°, respectively, while the diffraction pattern of the BTC framework disappears. This change indicates the recrystallization of $Cu^{2+}$ nodes into the metallic phase, accompanied by the decomposition of the ordered organic linkers at this temperature.

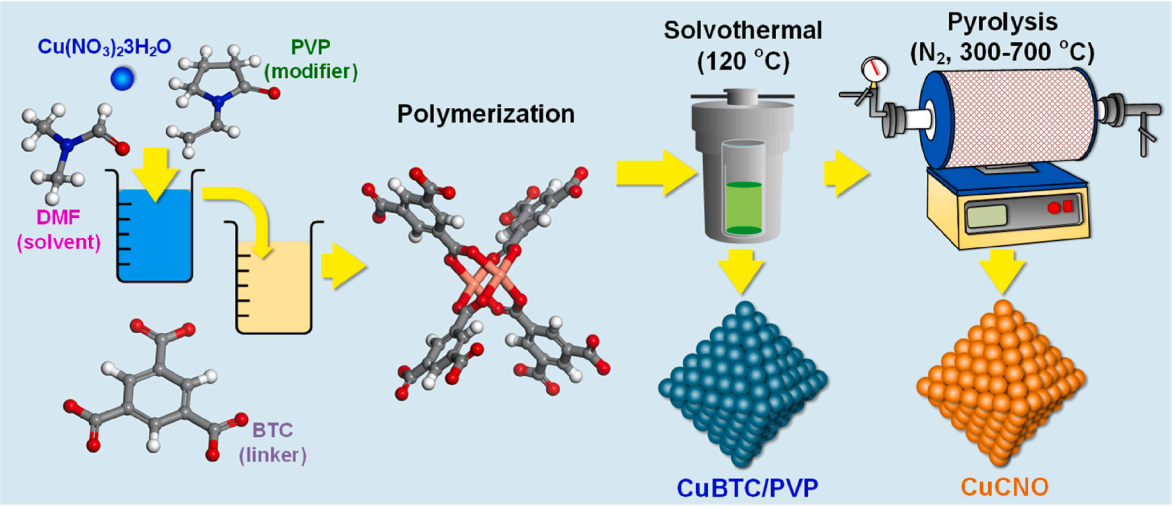


**Scheme 1.** Synthesis of CuBTC/PVP and CuCNO.

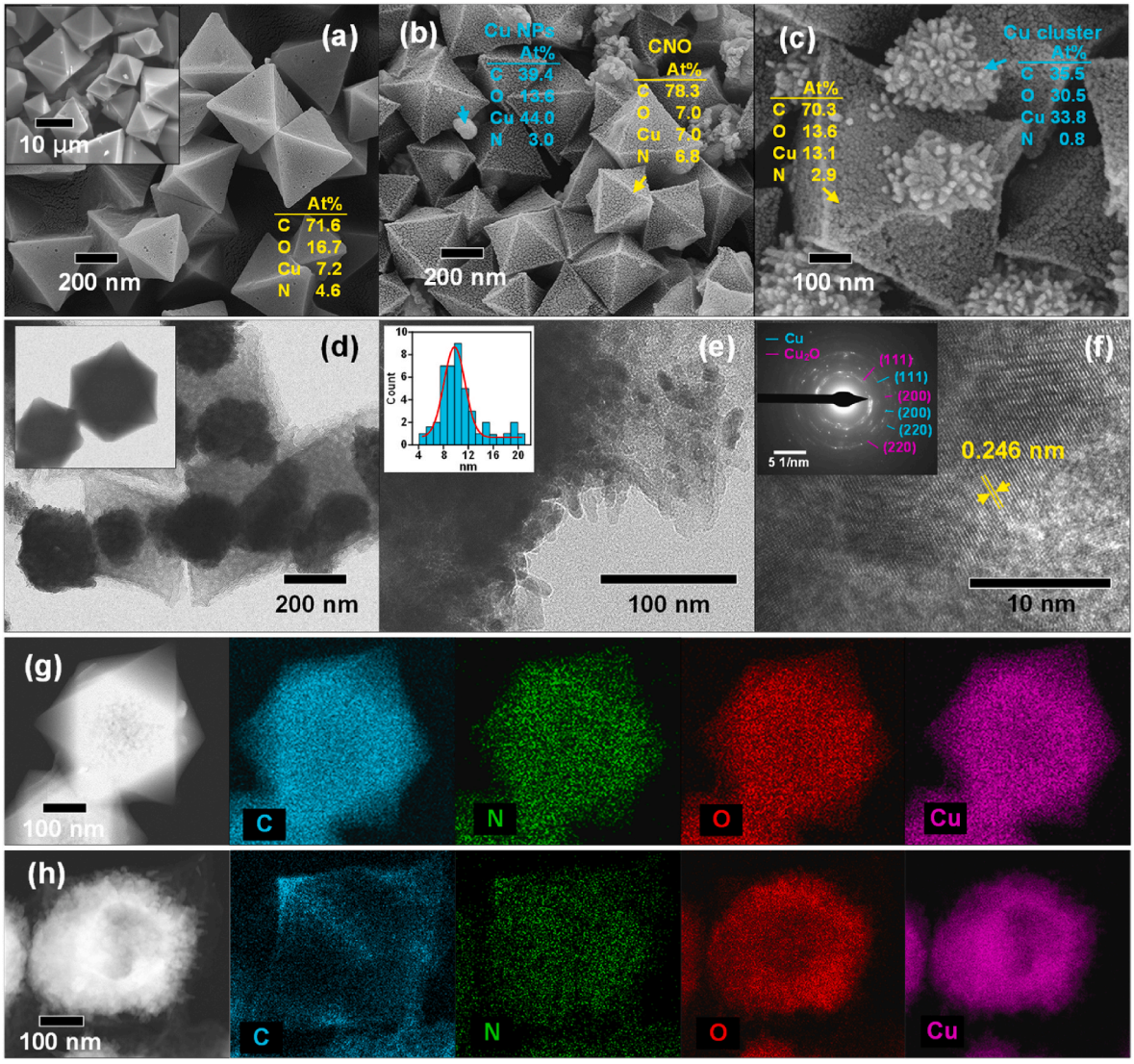


**Fig. 1.** SEM images of (a) CuBTC/PVP, (b) CuCNO(400), and (c) CuCNO(700); TEM of (d) CuCNO(400) and (e) nanorodes in the Cu cluster. (f) SAED and HRTEM of CuCNO(400). Elemental mappings of (g) CuBTC/PVP and (h) CuCNO(400).

Further pyrolysis at 400–700 °C results in the transformation of Cu metal into $Cu_2O$ (Pn $\bar{3}$ m, space group 224) and CuO (Tenorite, *C*2/*c*, space group 15) phases, with increased crystallinity evidenced by the intensified diffraction signals. Notably, the carboxyl groups in BTC molecules provide internal oxygen for the formation of Cu oxides even under an inert $N_2$ atmosphere. Thermogravimetry analysis (Fig. 2b) shows that an initial weight loss of ~25 % at 200 °C corresponds to the vaporization of crystalline water. A sharp mass decline centered at 300 °C highlights the decomposition of the copper tricarboxylate integrity. Above 400 °C, the BTC linkers fully carbonize into CNO, while Cu transitions to their oxygenated forms, as reflected in the XRD analysis. FTIR spectra in Fig. 2c evidence characteristic vibrations of BTC functional groups within 700–1700 nm, including C–H and C═C stretching in benzene rings at 764 and 1650 $cm^{-1}$, respectively, as well as carboxylate bending and stretching at 1450 $cm^{-1}$ and 1375 $cm^{-1}$, respectively [25]. The peak at 489 $cm^{-1}$ identifies $Cu^{2+}$ - ligand coordination in CuBTC [26], while the C–N bond at 1115 $cm^{-1}$ is specifically attributed by the PVP additive [27]. In pyrolyzed samples, the simplified patterns retain prominent C═C, C–O, and C–N signals and indicate the transformation of the BTC polymer into a graphitic carbon matrix in CuCNO. Concurrently, $Cu^{2+}$ precipitates as oxide $Cu_2O$ (630 $cm^{-1}$) and CuO (521 $cm^{-1}$) [28]. Raman shifts of CuBTC/PVP (Fig. 2d) display peaks below 600 $cm^{-1}$, associated with the stretching vibrations of $Cu^{2+}$-O in the framework. For CuCNO samples, two characteristic bands at 1302 $cm^{-1}$ and 1571 $cm^{-1}$, assigned to the defective $sp^3$-bonded (D) and $sp^2$ graphitic vibrations (G), respectively, indicate the formation of inorganic carbon crystallinity. The decreasing D-to-G peak intensity ratio ($I_D/I_G$) with increasing temperature suggests an enhancement in graphitic ordering [29]. On the other hand, in CuCNO(400), the sharp $E_g$ mode at 590 $cm^{-1}$ confirms the thermal reduction of $Cu^{2+}$ nodes to $Cu_2O$. This peak shifts to 278 $cm^{-1}$ ($A_g$) in CuCNO(700) due to the further oxidation of $Cu_2O$ to CuO [30], consistent with observations from XRD and FTIR analyses.

The BET adsorption isotherm of CuBTC/PVP (Fig. 2e) reveals a high specific surface area (S.S.A.) exceeding 800 $m^2\ g^{-1}$. However, carbonization leads to collapse of the BTC framework, drastically reducing the S.S.A. to below 100 $m^2\ g^{-1}$ in CNO samples. The isotherm of CuBTC/PVP exhibits an H4-type hysteresis loop, indicative of microporosity with narrow slit-like pores, based on IUPAC classification [31]. The hysteresis loop shifts to an H2-type on CuCNO(400) and CuCNO(700), implying capillary condensation of $N_2$ in ink-bottle mesopores formed by particle agglomerates. Pore size distribution (Fig. 2f) defines a micropore diameter of 2.2 nm in CuBTC/PVP, whereas CuCNO shows an increased mesopore fraction, with an average size peaking at 13 nm in CuCNO (400). This indicates the development of a carbon skeleton with

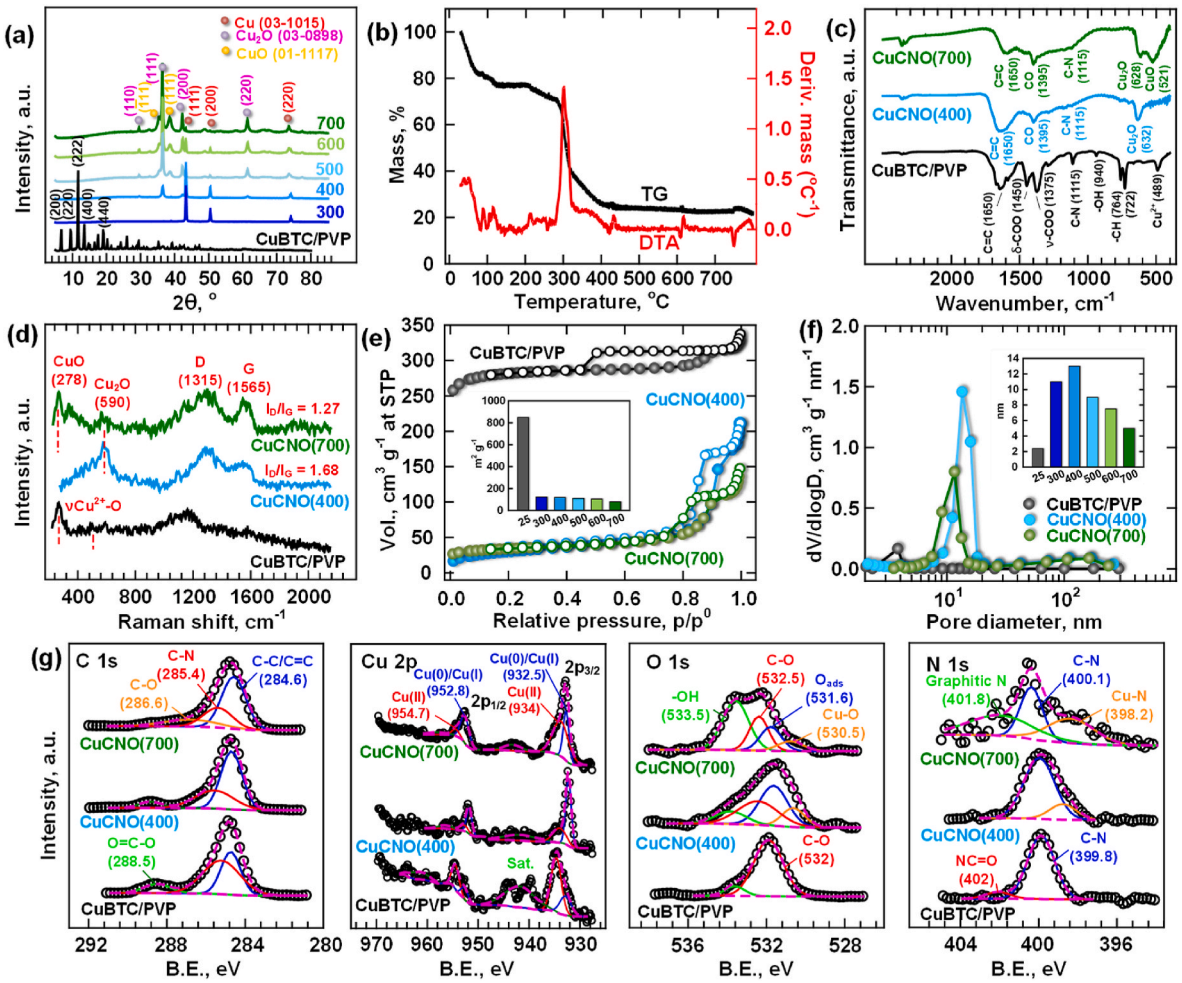


**Fig. 2.** (a) XRD and (b) thermal analysis of CuBTC/PVP. (c) FTIR, (d) Raman spectra, and (e) BET isotherms of CuCNO pyrolyzed at different temperatures, with corresponding (f) pore size distribution. (g) XPS at binding energies of C 1s, Cu 2p, O 1s, and N 1s orbitals.

expanded pore structures during BTC decomposition, despite the overall decrease in S.S.A. due to structural densification and loss of framework order. The full XPS spectra of CNO pyrolyzed at different temperatures in Fig. S1a show characteristic binding energies at approximately 285 eV, 400 eV, 530 eV, and 935 eV for C 1s, N 1s, O 1s, and Cu 2p, respectively [32]. The attenuation in O and N orbitals with increasing temperature, as shown in Fig. S1b, indicates the thermal decomposition of oxygenated and nitrogen-containing groups within the carbon matrix in CNO. Chemical states are quantified through peak deconvolution in Fig. 2g. Carboxyl group (O–C═O, 288.5 eV) from the BTC linker vanishes in CuCNO, while the signal for C–C/C═C (284.6 eV) is intensified, and those for C–N (285.4 eV) and C–O (286.6 eV) are weakened, reflecting carbonization effects [33]. In Cu $2p_{3/2}$ bands, $Cu^{2+}$ (934 eV), originally dominant in CuBTC, is largely reduced to zero-valent $Cu^0$ (932.5 eV) in CuCNO(400), while partially recrystallizing as CuO in CuCNO(700) [34]. The O 1s evolves from –COOH (532 eV) coordination in CuBTC/PVP to contributions from lattice oxygen (Cu–O, 530.5 eV) in oxides and adsorbed $O_{ads}$ (531.6 eV) in CNO, the latter sometimes linked to oxygen defects. Although missing oxygen atoms are not detectable via ex-situ photoelectron spectroscopy, $O_{ads}$ is often used as a proxy for surface defects [35]. N doping is evidenced by the replacement of C–N (399.8 eV) from PVP additive with graphitic-N (401.8 eV) and other nitride species such as Cu–N (398.2 eV) and C–N (400.1 eV) [36]. As summarized in Fig. S1c, the thermal evolution of chemical states with temperature results in nitrogen-doped carbon composites with embedded Cu oxide nanoparticles.

### 3.2. Electrochemical behaviors

Within the potential range where electrical double-layer capacitance ($C_{dl}$) dominates, the increased non-Faradaic current densities indicate an enhancement in electrochemical surface area (ECSA) for charge storage. Fig. 3a reveals that the voltammetry responses of CuCNO outperform those of the pristine CuBTC/PVP and bare glassy carbon electrode. This result contrasts with the trend of the BET surface area, implying the less accessibility of microporosity in CuBTC/PVP for electrochemical processes. When the BTC polymer converts to CNO, mesoporous surfaces promote more effective ion diffusion and sorption, despite the drastic decrease in S.S.A. Fig. 3b demonstrates the dependence of peak currents ($I_p$) on scan rate for the ferricyanide redox couple (in 0.1 M KCl), allowing estimation of ECSA based on the Nernst's theory [37]:

$$I_p = 269,000 n^{3/2} (ECSA) C (D_{Fe} \nu)^{1/2} \quad (1)$$

where n = 1 for $Fe(CN)_6^{3-} \rightleftharpoons Fe(CN)_6^{4-}$, C is the $K_3Fe(CN)_6$ concentration ($5 \times 10^{-6}$ mol $cm^{-3}$), $D_{Fe}$ is the diffusion coefficient ($7.6 \times 10^{-6}$ $cm^2$ $s^{-1}$), and $\nu$ is the scan rate (0.05 V $s^{-1}$). ECSA, determined from the slope of $I_p$ versus $\nu^{1/2}$, is summarized in Fig. 3c, alongside $C_{dl}$ values measured using the integrated method [38]:

$$C_{dl}(F) = \frac{1}{\nu \Delta V} \int_{V_1}^{V_2} I dV \quad (2)$$

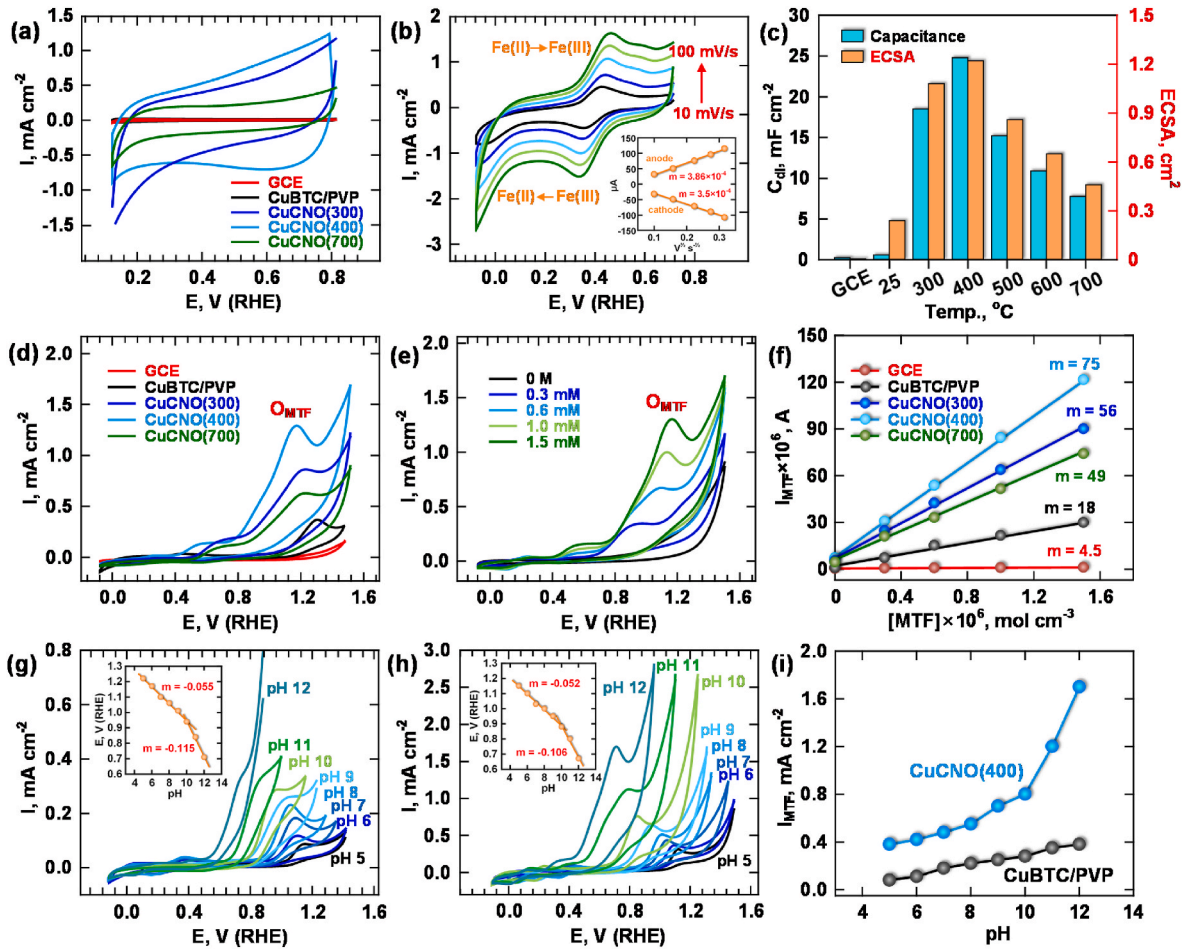


**Fig. 3.** (a) Capacitive currents of CuBTC/PVP and derived CuCNO electrodes measured in 1 M KOH (100 mV $s^{-1}$), (b) cyclic voltammetry of CuCNO(400) in 5 mM ferricyanide ($K_3Fe(CN)_6$, 0.1 M KCl). (c) Electrical capacitance and ECSA as affected by pyrolysis temperatures. (d) CV of CuBTC/PVP and derived CuCNO electrodes within 1 mM MTF, and (e) effect of MTF concentration on voltammetry of CuCNO(400) (0.1 M PBS, v = 50 mV $s^{-1}$, uncontrolled pH). (f) $O_{MTF}$ peak current ($I_{MTF}$) as a function of MTF molarity. Effect of pH on voltammetry of (g) CuBTC/PVP and (h) CuCNO(400), and (i) current densities of $I_{MTF}$ (MTF = 300 μM).

where $\Delta V = 0.7$ V. The ECSA of CuCNO(400) reaches 1.22 $cm^2$, almost 20 times that of the bare GCE (0.071 $cm^2$). Importantly, both ECSA and $C_{dl}$ peak at CuCNO(400), then tend to decline at higher temperatures, likely due to the coarsening of Cu nanoparticles, which reduces the density of active sites.

The electrochemical reactivity of the GCE and CuBTC/PVP toward metformin (MTF) is confirmed via voltammetry, as shown in Fig. S2. While $O_{MTF}$ intensity remarkably improves on CuBTC/PVP, relative to the GCE electrode, the $Cu^{2+}$ nods in the organic framework are deemed to the active sites facilitating electron transfer for the adsorbed metformin molecules. Pyrolyzing CuBTC to CuCNO further amplifies the $O_{MTF}$ response, as displayed in Fig. 3d, with CuCNO(400) exhibiting the most pronounced response (0.1 M PBS, 50 mV $s^{-1}$, pH 7–8, uncontrolled). This suggests that the transformation of $Cu^{2+}$ into with well-dispersed Cu oxides anchored on carbon octahedrons is critical to the high sensitivity of MTF detection. On the other hand, the Nicholson and Shain model describes the relationship between the Faradaic current and the concentration of electroactive species by assuming a diffusion-controlled redox process [39]. Accordingly, the anodic current density of the CuCNO(400) electrode at approximately +1.0 V ($O_{MTF}$) increases with rising MTF concentration, as present in Fig. 3e. The irreversible $O_{MTF}$ peak is then evaluated using:

$$I_{MTF} = 299,000n(ECSA)[MTF](\alpha D_{MTF}\nu)^{1/2} \quad (3)$$

where $D_{MTF}$ represents the diffusion coefficient of MTF ($5.6 \times 10^{-6}$ $cm^2$ $s^{-1}$) and $\alpha$ is the transfer coefficient, estimated from the peak potential $E_p$ and half-peak potential $E_{p/2}$ with $\alpha = \frac{0.0477}{|E_p - E_{p/2}|}$ [40]. The number of electrons (n) involved in the $O_{MTF}$ step is predicted via linear fitting of peak current $I_{MTF}$ versus [MTF] in mol $cm^{-3}$, as shown Fig. 3f. Given ECSA in Fig. 3c, the calculated n ranges from 1.8 to 2.1 for different electrodes, indicating a nearly two-electron oxidation process.

To further investigate the MTF sensing mechanism, voltammetry measurements are performed across a pH range of 5–12 using both CuBTC/PVP and CuCNO(400) electrodes, as shown in Fig. 3g and h, respectively. The $O_{MTF}$ peak potentials shift negatively with increasing pH due to the electrochemical thermodynamics. Linear regression of peak potential against pH yields a slope of $-\frac{2.3bRT}{nF}$ or $-0.059\frac{b}{n}$ V per pH, where $b$ represents the proton equivalence involved in the redox reactions [41]. The obtained slopes in the insets are −0.055 V/pH for CuBTC/PVP and −0.052 V/pH for CuCNO(400), which increase to −0.115 and −0.106 V/pH, respectively, at pH > 10. This trend suggests a two-proton process in MTF oxidation, increasing to four protons in alkaline conditions. Meanwhile, a sharp increase in $O_{MTF}$ peak current occurs around pH 10 on CuCNO(400), but not for CuBTC/PVP (Fig. 3i). MTF, a diprotic Brønsted acid, has two dissociation constant, $pK_{a1} = 2.8$ and $pK_{a2} = 11.5$ (Fig. 4a) [42]. At higher pH, deprotonation of $=NH_2^+$ groups reduces electrostatic repulsion between MTF and $Cu^{2+}$-exposed surfaces, thereby enhancing the Faradaic current response. Electrostatic potential (ESP) simulation elucidates the intermolecular charge distribution, which reveals a predominant negativity around the two amine

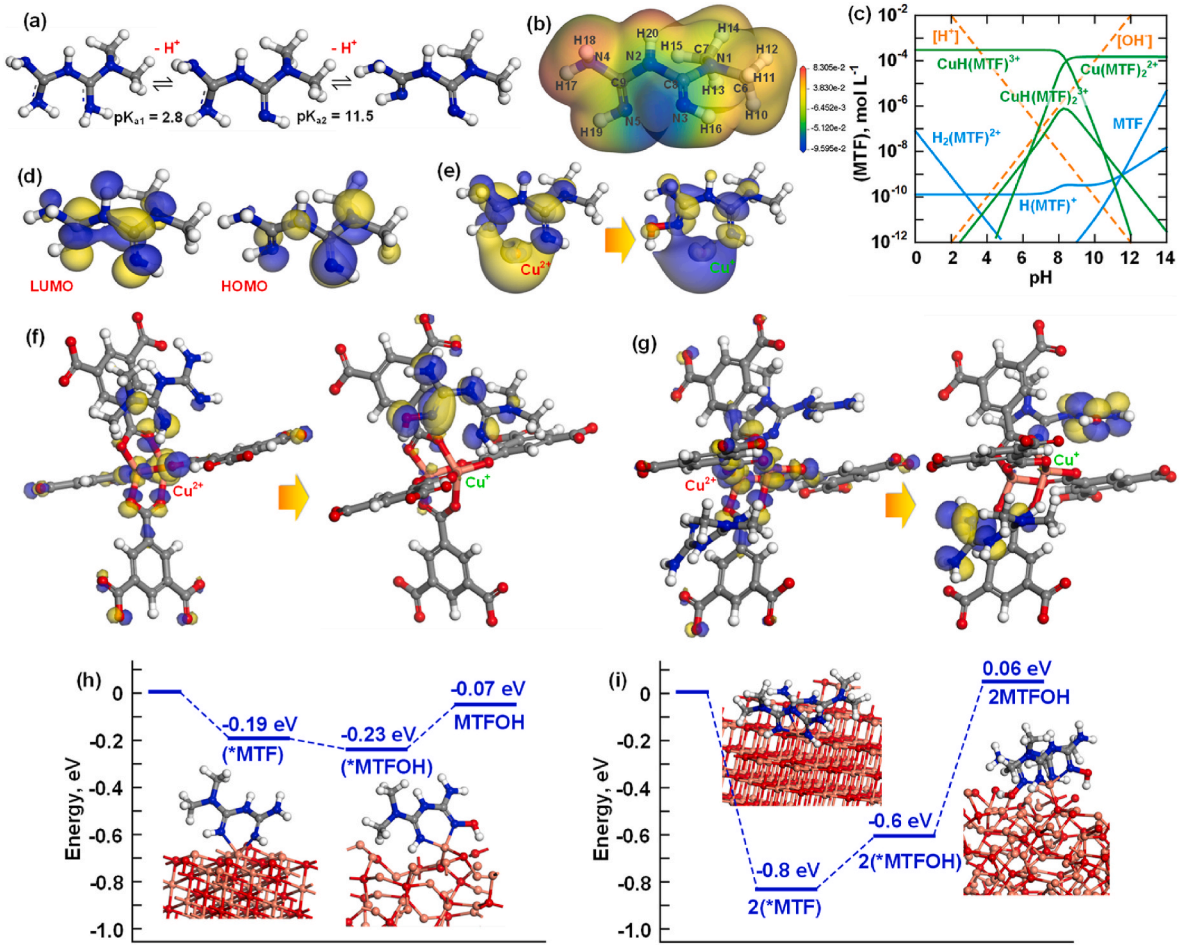


**Fig. 4.** (a) Acid-base equilibrium and (b) electrostatic potential of metformin. (c) Speciation of $Cu^{2+}$-MTF complexes in the presence of $5 \times 10^{-4}$ M MTF and 1 M total Cu(II). (d) LUMO and HOMO of metformin, (e) HOMO of $Cu^{2+}(C_4H_{11}N_5)$ and $Cu^{+}(C_4H_{10}N_5OH)$ (isosurface value = 0.03 electron/Å). (f) Optimal structures of $CuBTC(C_4H_{11}N_5)$ and $CuBTC(C_4H_{10}N_5OH)$, and (g) $CuBTC(C_4H_{11}N_5)_2$ and $CuBTC(C_4H_{10}N_5OH)_2$. Energy difference of MTF and MTFOH adsorption on CuO and $Cu_2O$ sites, respectively, in forms of (h) mono-complex and (i) double complex.

(=NH) groups (N3 and N5), as shown in Fig. 4b. $Cu^{2+}$ ions function as Lewis acid sites, coordinating with these = NH to form a biguanide complex [43,44]. On the other hand, at pH > 9, the number of ligand in the complex doubles as $[Cu^{2+}(C_4H_{11}N_5)_2]$ ($Cu^{2+} + 2C_4H_{11}N_5 \rightleftharpoons Cu^{2+}(C_4H_{11}N_5)_2$; $\beta_3 = 10^{22.2}$) [45]. The acid-base thermodynamics and equilibrium constants governing $Cu^{2+}$-MTF speciation are detailed in the Supporting Information S3, where total MTF concentration influences the complexation profiles as a function of pH (Fig. 4c & Fig. S3). Accordingly, the pronounced shift in the pH-dependent $O_{MTF}$ peak potential at high pH is attributed to enhanced bidentate chelation of MTF on Cu oxide surfaces, effectively doubling the coordination sites.

DFT calculations predict the molecular orientation of biguanide during electrooxidation (see Supporting Information S4 for full energy density simulations). As shown in Fig. 4d, analysis of the highest occupied molecular orbital (HOMO) and the lowest unoccupied molecular orbital (LUMO) for MTF highlights electron-rich (blue) and –deficient (yellow) regions [46]. Fukui indices, $f^+$, identify nucleophiles attack-prone sites, particularly one of the = NH groups, suggesting that MTF oxidation initiates via hydrolytic attack by $OH^-$ (Fig. S4) [47]. Within the complex, Lewis acid–base interactions dominate, with electron depletion at $Cu^{2+}$ evident from the HOMO distribution, rendering them susceptible to reduction (Fig. 4e) [48]. Conversely, the N3 and N5 atoms in MTF are the most vulnerable for oxidation, leading to a two-electron, two-proton transfer mechanism (=NH + $H_2O \rightleftharpoons$ –NOH + $2H^+ + 2e^-$). Under anodic polarization, an electron-rich $Cu^+$ catalytic state forms so that promotes metal-ligand charge transfer.

$$Cu^{2+}(C_4H_{11}N_5) + H_2O \rightarrow Cu^{+}(C_4H_{10}N_5OH) + 2H^+ + e^- \quad (4a)$$

$$Cu^{+} \rightarrow Cu^{2+} + e^- \quad (4b)$$

$$Cu^{2+}(C_4H_{11}N_5) + H_2O \rightleftharpoons Cu^{2+}(C_4H_{10}N_5OH) + 2H^+ + 2e^- \quad (4c)$$

In this scenario, $Cu^{2+}$ nodes in CuBTC/PVP, characterized by high $f^-$ mapped electron density and thus vulnerability to electrophilic attach (Fig. S5), serves as the primary mediators (Fig. 4f). At high pH, bidentate coordination facilitates a two-electron, four-proton process (Fig. 4g):

$$Cu^{II}BTC(C_4H_{11}N_5)_2 + 2H_2O \rightleftharpoons Cu^{0}BTC(C_4H_{10}N_5OH)_2 + 4H^+ + 2e^- \quad (5)$$

In the case of pyrolyzed CuCNO, nucleophilic attack targets the HOMO of MTF with high probability of donating electrons to the CuO surface:

$$CuO - (C_4H_{11}N_5) + H_2O \rightleftharpoons CuO - (C_4H_{10}N_5OH) + 2H^+ + 2e^- \quad (6a)$$

$$CuO - (C_4H_{11}N_5)_2 + 2H_2O \rightleftharpoons Cu_2O - (C_4H_{10}N_5OH)_2 + 4H^+ + 2e^- \quad (6b)$$

The Forcite module was employed to rapidly pre-optimize the molecular structures of CuBTC and MTF. Subsequently, the total free energies, HOMO, and LUMO (Table S1) of *MTF and *MTFOH species adsorbed on Cu sites within CuCNO composite were computed using the $DMol^3$ module. Based on electrochemical analyses and operando spectroscopic results, under anodic potentials the $O_{MTF}$ process is

catalytically mediated by a CuO/$Cu_2O$ transition, which participates the multiple electron-proton transfer of MTF oxidation. The energy states of *MTF and its intermediate *MTFOH adsorbed on the corresponding oxide surface, CuO and $Cu_2O$, in (1 1 1) system (Fig. S6), are computed. The pH-dependent voltammetric responses shown in Fig. 3i suggested that the binding configurations of both monomeric and dimeric biguanide species significantly influenced the strength of MTF adsorption onto Cu oxides. Fig. 4h and i summarize the calculated free energies of adsorbed *MTF species, which predict the energetic stability of monomeric and dimeric forms at $O_{MTF}$ step. Notably, the oxidation of dimeric *MTF to *MTFOH proceeds through an uphill transition during CuO-to-$Cu_2O$ recrystallization, in contrast to the monomeric forms. This result implies that oxidation in the dimeric coordination may be relatively reversible at higher pH conditions. Moreover, the high energy barrier associated with desorption of doubly chelated $C_4H_{10}N_5OH$ into the aqueous solution underscores the strong surface interaction and high selectivity of CuCNO for MTF detection.

Fig. 5a and b presents the operando Raman spectra of CuBTC/PVP and CuCNO(400) electrodes in the presence of 10 mM MTF at increasing potentials. The disappearance of $Cu^{2+}$ signals in CuBTC above +0.7 V is attributed to anodization, coinciding with the onset of MTF oxidation. In the meantime, N–H deformation near 650 and 780 $cm^{-1}$, along with saturated amine vibrations at 950 $cm^{-1}$, verifies the adsorption of MTF and its hydrolyzed intermediates [49]. On CuCNO(400), the $E_g$ mode of $Cu_2O$ at around 590 $cm^{-1}$ persists between +0.1 V and +0.7 V. Beyond +0.8 V, the emergence of characteristic vibrations at 380, 507, 583 $cm^{-1}$ corresponds to the formation of the $Cu_4O_3$ phase, a mixed-valence $Cu_2O$–CuO composite [50]. This spectral evolution aligns with voltammetry findings, which support the partial oxidation of $Cu_2O$ to CuO during MTF catalytic oxidation.

Notably, the $O_{MTF}$ peak shifts with increasing MTF concentrations, as shown in Fig. 3e and Fig. S2, which can be attributed to electrode kinetics. The Faradaic current is often limited by diffusion, in which the redox rate depends on how rapidly MTF molecules reach active sites from bulk solution. For an irreversible or quasi-reversible electron transfer processes, however, high potentials are required to fully polarize the electrode surface at elevated concentrations, as the system becomes less influenced by the activation rate [51]. To diagnose the diffusion-controlled kinetics of the $O_{MTF}$ step, the redox behavior is analyzed using Nernst's model, which predicts a linear dependence of the peak potential on $v^{1/2}$ [52].

$$E_p = E^{0'} - \frac{RT}{\alpha n F}\left[0.78 + \ln\left(\frac{D_{MTF}^{1/2}}{k^0}\right) + \ln\left(\frac{\alpha n F}{RT}\right)^{1/2} v^{1/2}\right] \quad (7a)$$

Given $\alpha = \frac{0.0477}{|E_p - E_{p/2}|}$, the heterogeneous electron transfer rate constant ($k^0$) is simplified as:

$$k^0 = 2.415 \exp\left[-0.02\frac{F}{RT}\right] D_{MTF}^{1/2}\left(E_p - E_{p/2}\right)^{-1/2} v^{1/2} \quad (7b)$$

or at 298 K:

$$k^0 = 1.11 D_{MTF}^{1/2}\left(E_p - E_{p/2}\right)^{-1/2} v^{1/2} \quad (7c)$$

Voltammetry data of MTF (Fig. S7) at varying scan rates reveal that $O_{MTF}$ peaks scale with $v^{1/2}$, as shown in Fig. 5c. The linear regression slope is used to determine $k^0$ values, which follow the order: CuCNO (400) (0.047 cm s-1) > CuBTC/PVP (0.034 cm s-1) > CuCNO(700) (0.022 cm s-1). Cu2O, formed at 400 °C, is the most active phase for direct electron transfer reactions. To assess the charge transfer efficiency, the impedance spectroscopy of MTF oxidation was performed at +1.0 V (vs. RHE, [MTF] = 10 mM). Nyquist plots in Fig. 5d are fitted using the inset equivalent circuit, which consists of a charge transfer resistance ($R_{CT}$) in parallel with an electrical capacitance ($C_{dl}$) or a constant phase element (CPE), and an electrolyte resistant ($R_S$) in series. The extracted $R_{CT}$ values rank as follows: CuCNO(400) (82 Ω) < CuCNO (700) (221 Ω) < CuBTC/PVP (298 Ω). (The detailed EIS parameters are provided in Table S2.) $R_{CT}$ refers to the resistance encountered at Cu sites during the MTF redox process. As summarized in Fig. 5e, the inverse relationship between the rate constant $k^0$ and $R_{CT}$ indicates the superior electron transfer kinetics of CuCNO(400). EPR spectroscopy ascertains the presence of surface oxygen vacancies. As illustrated in Fig. 5f, EPR signal is absent on CuBTC/PVP. In contrast, oxygen vacancies ($O_V$) are identified on CuCNO materials with a g-value of 1.998 due to unpaired electrons trapped at these defects. CuCNO(400) presents the most intense $O_V$ signals [53],consistent with the elevated $O_{ads}$

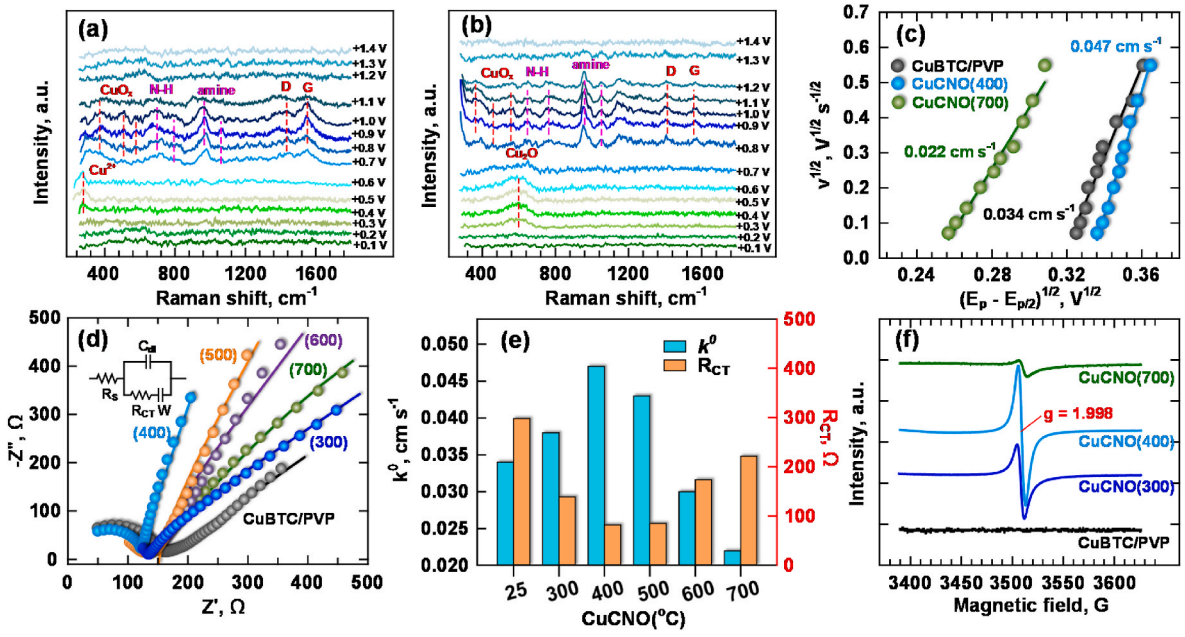


**Fig. 5.** Operando Raman spectroscopy of (a) CuBTC/PVP and (b) CuCNO(400) during scanning anode potentials in the presence of MTF (0.1 M PBS, pH 10). (c) $O_{MTF}$ peak potential in $(E_p - E_{p/2})^{1/2}$ as affected by square root of scan rate (0.5 mM MTF, 0.1 M phosphate buffer). (d) Impedance analysis at +1.0 V (vs. RHE), and (e) rate constants and charge transfer resistances of different CuCNO electrodes. (f) EPR analysis in the region of oxygen vacancy.

content in the O 1s XPS spectra (Fig. 2g). Pyrolysis at 400 °C, according to XRD analysis, results in the formation of $Cu_2O$ phase developed from metallic Cu (Fig. 2a). The presence of Cu(0)/Cu(I) mixed-valence state enriches oxygen defects in the CNO structure, which improves electron mobility and thereby increases catalytic activity for MTF oxidation, as corroborated in both impedance and heterogeneous rate analyses [54]. Recrystallization into CuO with a more ordered lattice occurs at higher temperature, eliminating $O_V$ defects, as evident in CuCNO(700).

### 3.3. Electrochemical sensing of metformin

To minimize interference from capacitive currents and enhance sensitivity for trace pollutant detection, MTF analysis was performed using differential pulse voltammetry (DPV). Fig. 6a–c displays the DPV curves of CuBTC/PVP, CuCNO(400), and CuCNO(700) electrodes in 0.1 M phosphate buffer (pH 10) with increasing MTF concentrations (0.5–300 μg $L^{-1}$). The $O_{MTF}$ peak currents ($I_p$) are recorded at lower potentials on CuCNO(400) (+0.85 V) compared to CuBTC/PVP (+0.92 V) and CuCNO(700) (+0.97 V). Plots of $I_P$ versus MTF molarity exhibit two linear ranges: 0.5–50 μg $L^{-1}$ (low) and 50–300 μg $L^{-1}$ (high), as shown in Fig. 6d and e, respectively. In dynamic potential analysis (CV or DPV modes), charge transfer efficiency increases at low analyte concentrations due to the greater availability of active sites for redox reactions. Therefore, the enhanced ECSA utilization improves current selectivity concerning concentration changes, as well as the limit of detection (LOD). The slope of $I_P$ vs. [MTF] for CuCNO(400) is 0.793 μA L $\mu g^{-1}$ (or 102 μA $\mu M^{-1}$, $R^2 = 0.997$), surpassing CuBTC/PVP (0.175 μA L $\mu g^{-1}$, $R^2 = 0.993$) and CuCNO(700) (0.367 μA L $\mu g^{-1}$, $R^2 = 0.994$). The LOD and limit of quantification (LOQ), calculated using $LOD = \frac{3\sigma}{m}$ and $LOQ = \frac{10\sigma}{m}$ [55], where $\sigma$ is the standard deviation of capacitive currents at $O_{MTF}$ ($1.45 \times 10^{-8}$ A for 10 replicates) and $m$ is the sensitivity (μA L $\mu g^{-1}$), are determined to be 0.054 μg $L^{-1}$ and 0.183 μg $L^{-1}$, respectively. Fig. 6f gathers the sensitivities of electrochemical MTF sensing across different CuCNO electrodes. Both calibration slopes for low and high MTF levels are maximized with CuCNO(400). This result confirms that Cu(I) nanoparticles embedded in mesoporous carbon matrix is of benefit to sensing sensitivity. Cu oxide aggregation at high temperatures (e.g., CuCNO(700)) reduces the number of accessible active sites, leading to diminished redox response.

To assess the practical applicability of CuCNO(400) electrode, MTF detection was conducted in various real water samples collected from Kaohsiung City, Taiwan, including Chengcing Lake water (CCL), Love River water (LR), and wastewater treatment plant effluent (WWTP). The chemical compositions of these samples are listed in Table S3, with

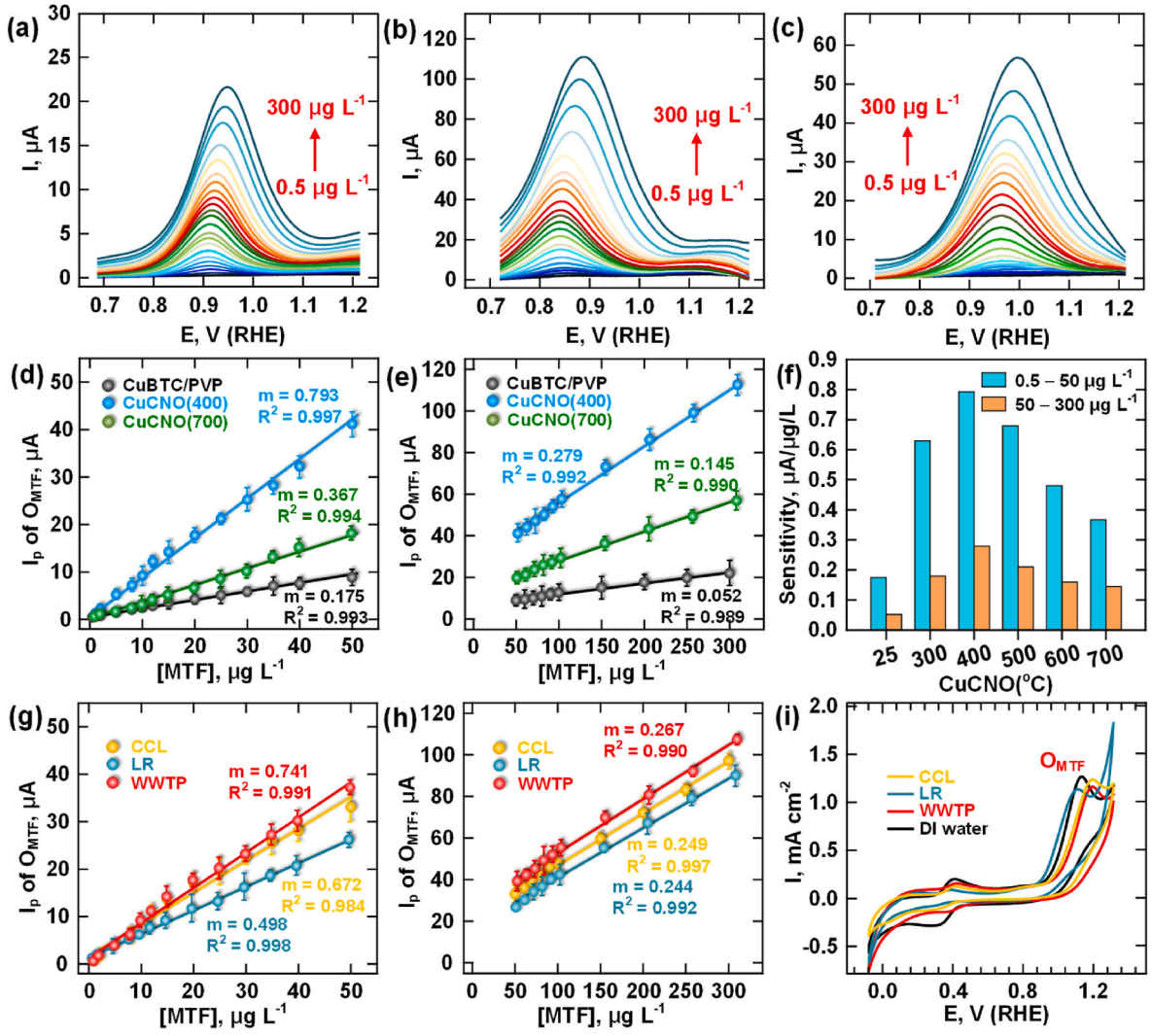


**Fig. 6.** DPV analyses of (a) CuBTC/PVP, (b) CuCNO(400), and (c) CuCNO(700), and corresponding linearity of peak current versus MTF molarity in the range of (d) 0.5–50 μg $L^{-1}$ and (e) 50–300 μg $L^{-1}$. (f) Sensitivity of CuCNO electrodes as a function of pyrolysis temperatures. Peak currents versus MTF molarity in the range of (g) 0.5–50 μg $L^{-1}$ and (h) 50–300 μg $L^{-1}$ in different water samples (CCL: Chengcing Lake water; LR: Love River water; WWTP: wastewater treatment plant effluent). (i) CV of CuCNO(400) in real-world waters.

corresponding DPV analyses presented in Fig. S8. At low MTF concentrations, the CuCNO(400) electrode maintains high sensitivity in lake water (0.741 μA L μg$^{-1}$) and wastewater effluent (0.672 μA L μg$^{-1}$), but a moderate decrease is observed in river water (0.498 μA L μg$^{-1}$) (Fig. 6g). In contrast, at higher concentrations, water matrix effects are negligible, with an average sensitivity of 0.24 μA L μg$^{-1}$, comparable to 0.279 μA L μg$^{-1}$ in 0.1 M phosphate buffer (Fig. 6h). These variations are attributed to differences in ionic strength, with river water exhibiting the highest value of 0.68 eq L$^{-1}$ (classifying it as a brackish water). Increased salinity, primarily due to the high chloride ion concentration, contributes to competitive adsorption at Cu sites, thereby hindering MTF binding and lowering surface reactivity. Fig. 6i illustrates the CV profiles of 1 mM MTF in different water samples. The Faradaic currents associated with $O_{MTF}$ remain largely unchanged, indicating that background electrolytes introduce insignificant side reactions. However, the $O_{MTF}$ peak resolution may be compromised, as the overpotential required for concurrent water splitting decreases at high salinity conditions.

A comprehensive summary of electrochemical methods for metformin quantification is provided in Table S4. Earlier approaches relied on soluble $Cu^{2+}$ in acetate buffers to form $Cu^{2+}$-biguanide complexes, which were electrochemically detectable on various carbon materials [56–59] and metal oxides, [60,61]. However, the use of copper salts or complexes may contaminate the target samples, raising environmental concerns due to the potential generation of copper-containing wastewater. Group XI metals – including Cu, Ag, and Au – have been explored for MTF sensing [8,62–64]. These coinage metals possess partially filled d-orbitals, functioning as Lewis acid centers for chelation and oxidation of MTF via metal-ligand charge transfer mechanisms. More recently, to improve stability and mitigate dissolution issues, metal organic frameworks have been used to immobilize $Cu^{2+}$ within crystalline architectures. Trimesic acid-based Cu-MOFs, when integrated with modifiers such as g-$C_3N_4$ [65], CNTs [66], or Nafion [67], can homogenize MOF particles and show better electrochemical responsiveness. In this study, pyrolysis of CuBTC/PVP proves to modulate the dispersion and electrochemical surface area of the resulting mesoporous metal-carbon composites, boosting the current response for MTF detection, especially in real-world waters.

The sensing reproducibility of the CuCNO(400) electrode was evaluated through 15 independent DPV measurements (n = 15, MTF = 2–10 μg L$^{-1}$). The mean recovery ($\overline{P}$) determined was used to calculate the standard deviation (*sd* for sample data) and establish the upper and lower warning limits ($\overline{P} \pm 2sd$) as well as the upper and lower control limits ($\overline{P} \pm 3sd$) for a quality control analysis [68]. Detailed calculations are provided in Table S5–S8. Fig. 7a exemplifies the control chart for quality assurance of DPV detection in river water, showing an average $\overline{P}$ of 99.2 % with a *sd* of 7.7 %. Comparable results are obtained in tap water ($\overline{P}$ = 100.1 %, *sd* = 6 %), lake water ($\overline{P}$ = 100.4 %, *sd* = 6.85 %), and wastewater treatment effluent ($\overline{P}$ = 101.8 %, *sd* = 6.65 %), as shown in Fig. S9a–S9c. The broader recovery corridor observed in river water around the centerline suggests greater scattered detection data. Nevertheless, all analytical values fall within defined UWL and LWL in real water samples, affirming the reliability and acceptable accuracy of metformin quantification. For comparison, the laboratory chromatography analysis (HPLC) yielded an average metformin recovery of 102 %

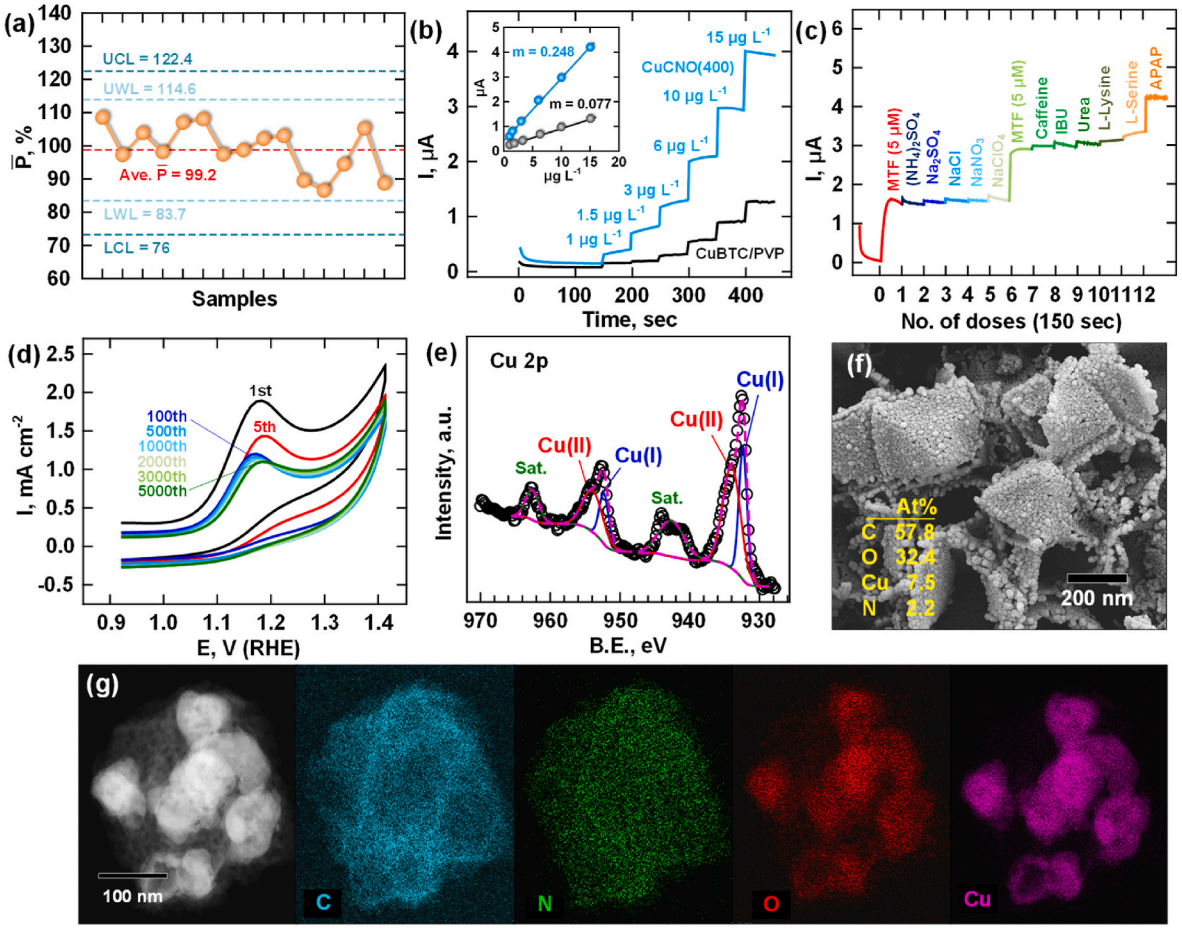


**Fig. 7.** (a) Quality control chart using CuCNO(400) for MTF detection in river water (n = 15, 2–10 μg L$^{-1}$). (b) MTF quantification with chronoamperometry mode, (c) as affected by different interference chemicals (+1.0 V vs. RHE). (d) Effect of voltammetry scans on MTF oxidation using CuCNO(400) electrode (MTF = 1 mM, v = 50 mV s$^{-1}$). (e) XPS at Cu 2p orbital, (f) SEM image, and (g) elemental mappings of the used CuCNO(400) electrode.

with a standard deviation of 8.95 % (Fig. S8d). Chronoamperometry was performed by successive additions of trace MTF at +1.0 V (vs. RHE), as shown in Fig. 7b. The staircase-shaped current increments confirms the catalytic response of electrodes to rising MTF concentration, with a sensitivity of 0.248 μA L $\mu g^{-1}$ on CuCNO(400), approximately three times higher than that of CuBTC/PVP (0.077 μA L $\mu g^{-1}$). The selectivity tests are further assessed on CuCNO(400) toward MTF (+1.0 V vs. RHE) through stepwise additions of inorganic salts (1 mM $(NH_4)_2SO_4$, $Na_2SO_4$, NaCl, $NaNO_3$, and $NaClO_4$) and organic compounds (100 μg $L^{-1}$ caffeine, ibuprofen, urea, lysine, serine, and acetaminophen), as shown in Fig. 7c. The presence of common anions ($SO_4^{2-}$, $Cl^-$, $NO_3^-$, and $ClO_4^-$) at millimolar levels does not obviously affect the current response. Conversely, organic substances, which frequently coexist with pharmaceuticals in wastewater, also exhibit minimal interference – except for acetaminophen (APAP). Due to its reversible redox reactions near +0.6 V on carbonaceous materials [69], varied APAP quantities may cause transient current fluctuations at high potentials, impacting MTF calibration. Fig. 7d displays the repetitive voltammetric scans in 1 mM MTF using CuCNO(400) electrode. After an initial stabilization within the first 10 scans, the $O_{MTF}$ peak current remains consistent at around 1.2 mA $cm^{-2}$, with a standard deviation of less than 5 %, over 100–5000 scans, confirming the sensor's durability and long-term stability. Post-electrolysis characterization indicates partial metal passivation, evidenced by an increase in the $Cu^{II}O$ phase (Cu 2p) from 20 % in the pristine electrode (Fig. 2g and Fig. S1) to 63 % after voltammetric cycling (Fig. 7e). This shift is accompanied by an increase in atomic ratio of O and noticeable growth in Cu clusters after electrolysis cycles, whereas the 3-D octahedral morphology of the carbon substrate remains intact (Fig. 7f). Elemental mappings in Fig. 7g reveal localized oxygen accumulation around CuO aggregates, distributed throughout the used CNO structure. These findings suggest that, although moderate Cu corrosion occurs due to prolonged electron transfer, the structural integrity and functionality of the composite electrode remain well preserved. Moreover, the change in the atomic ratio of total Cu in the used CuCNO(400) is insignificant compared to that of the original sample (Fig. 1a–b), indicating its minimal impact on both toxicity and effluent quality.

## 4. Conclusions

A Cu–N-enriched carbon composite was synthesized from the metal-organic framework, CuBTC/PVP, for electrochemical metformin quantification. During pyrolysis, $Cu^{2+}$ nodes recrystallized into well-dispersed Cu clusters embedded within a mesoporous carbon nano-octahedral architecture (CuCNO). Electrochemical analysis confirmed that the effective area, optimized in CuCNO(400), positively correlated with MTF sensing current density. In situ Raman spectroscopy revealed that MTF oxidation was mediated by Cu(II)/Cu(I) redox couple at +1.0 V. Free energy computations suggested a two-electron transfer mechanism, with oxidation of the biguanide amino (=NH) group to hydroxylamine (-NOH). Under alkaline conditions, MTF formed stable bidentate chelates with $Cu_2O$ sites, further increasing Faradaic response. DPV mode achieved a sensitivity of 0.793 μA L $\mu g^{-1}$ with a detection limit of 0.054 μg $L^{-1}$, demonstrating excellent analytical recovery and reproducibility. MTF quantification was validated in complex matrices containing common interfering chemicals and real-world water samples. The 3D copper-carbon composite in CuCNO electrode exhibited robust long-term stability and accuracy comparable to the conventional chromatography method for environmental monitoring.

## CRediT authorship contribution statement

**Yu-Jen Shih:** Writing – review & editing, Writing – original draft, Visualization, Validation, Supervision, Resources, Project administration, Methodology, Investigation, Funding acquisition, Conceptualization. **Zhi-Lun Wu:** Methodology, Investigation, Formal analysis, Data curation. **Wei-Hsiang Chen:** Data curation, Investigation, Methodology, Resources. **Yu-Hsuan Liu:** Validation, Methodology, Formal analysis, Data curation. **Chin-Pao Huang:** Conceptualization, Investigation, Methodology, Supervision.

## Declaration of competing interest

The authors declare that they have no known competing financial interests or personal relationships that could have appeared to influence the work reported in this paper.

## Acknowledgement

The authors would like to thank the National Science and Technology Council, Taiwan for generous finance support of this research project under Contract No. NSTC 111-2223-E-110 -003 -MY4.

## Appendix A. Supplementary data

Supplementary data to this article can be found online at https://doi.org/10.1016/j.carbon.2025.120705.

## References

[1] M. Patel, R. Kumar, K. Kishor, T. Mlsna, C.U. Pittman Jr., D. Mohan, Pharmaceuticals of emerging concern in aquatic systems: chemistry, occurrence, effects, and removal methods, Chem. Rev. 119 (6) (2019) 3510–3673, https://doi.org/10.1021/acs.chemrev.8b00299.

[2] R. Hernández-Tenorio, E. González-Juárez, J.L. Guzmán-Mar, L. Hinojosa-Reyes, A. Hernández-Ramírez, Review of occurrence of pharmaceuticals worldwide for estimating concentration ranges in aquatic environments at the end of the last decade, J. Hazard. Mater. Adv. 8 (2022) 100172, https://doi.org/10.1016/j.hazadv.2022.100172.

[3] A.B.A. Boxall, J.L. Wilkinson, A. Bouzas-Monroy, Medicating nature: are human-use pharmaceuticals poisoning the environment? One Earth 5 (2022) 1080–1084, https://doi.org/10.1016/j.oneear.2022.09.009.

[4] Y. Choi, J.H. Lee, K. Kim, H. Mun, N. Park, J. Jeon, Identification, quantification, and prioritization of new emerging pollutants in domestic and industrial effluents, Korea: application of LC-HRMS based suspect and non-target screening, J. Hazard. Mater. 402 (2021) 123706, https://doi.org/10.1016/j.jhazmat.2020.123706.

[5] P. Phogat, S. Sharma, R. Jha, S. Singh, Electrochemical sensors, in: Electrochemical Devices. Engineering Materials, Springer, Singapore, 2024, https://doi.org/10.1007/978-981-96-0527-9_5.

[6] E.P. Ambrosio-Albuquerque, L.F. Cusioli, R. Bergamasco, A. Ap S. Gigliolli, L. Lupepsa, B.R. Paupitz, P.A. Barbieri, L.A. Borin-Carvalho, A.L. de B. Portela-Castro, Metformin environmental exposure: a systematic review, Environ. Toxicol. Pharmacol. 83 (2021) 103588, https://doi.org/10.1016/j.etap.2021.103588.

[7] J.W. Lee, Y.J. Shin, H. Kim, H. Kim, J. Kim, S.A. Min, P. Kim, S.D. Yu, K. Park, Metformin-induced endocrine disruption and oxidative stress of Oryzias latipes on two-generational condition, J. Hazard. Mater. 367 (2019) 171–181, https://doi.org/10.1016/j.jhazmat.2018.12.084.

[8] A. Balakrishnan, M. Sillanpää, M.M. Jacob, D.V.N. Vo, Metformin as an emerging concern in wastewater: occurrence, analysis and treatment methods, Environ. Res. 213 (2022) 113613, https://doi.org/10.1016/j.envres.2022.113613.

[9] Y.J. Shih, Y.Q. Su, W.H. Chen, S.K. Lin, Y.C. He, C.P. Huang, Copper nanoparticles encapsulated in reduced graphene oxide electrode ($Cu_xrGO_{1-x}$) for the electrochemical quantification of metformin in water, Chem. Eng. J. 471 (2023) 144676, https://doi.org/10.1016/j.cej.2023.144676.

[10] Y. Dong, T. Li, H. Su, X. Zhang, J. Zhang, Cobalt-copper bimetallic selenides embedded in nitrogen-doped porous carbon nanocubes for diclofenac electrochemical sensing, J. Hazard. Mater. 477 (2024) 135281, https://doi.org/10.1016/j.jhazmat.2024.135281.

[11] T. Shaikh, S. Pise, R. Bhosale, M. Vadiyar, K.W. Nam, S. Kolekar, A review and perspective on advancement in metal–organic framework-based composites for supercapacitors: from dimensionalities to functionalities, Energy Fuels 39 (2025) 2396–2421, https://doi.org/10.1021/acs.energyfuels.4c05687.

[12] T.S. Priya, T.W. Chen, S.M. Chen, T. Kokulnathan, B.S. Lou, T. Algarni, W.A. Al-onazi, M.S. Elshikh, MIL-88A derived zerovalent iron embedded mesoporous carbon with carbon black composite based electrochemical sensor for the detection of metol, Carbon 223 (2024) 119026, https://doi.org/10.1016/j.carbon.2024.119026.

[13] J. Huang, Y. Xu, M. Liu, P. Jiang, X. Guo, T. Gan, C. Wu, K. Wu, Rapid room-temperature synthesis of disposable Co nanoparticles modified 3D N-doped porous carbon electrode device for efficient electrochemical detection of veterinary drug and pesticide residue, Carbon 219 (2024) 118806, https://doi.org/10.1016/j.carbon.2024.118806.

[14] J.N. Ballı, O. Gungor, M. Kose, A series of biguanide ligands and their Cu(II) complexes: cholinesterase inhibitory and antimicrobial properties, Chem. Biodiversity 21 (2024) e202301434, https://doi.org/10.1002/cbdv.202301434.

[15] E.Y. Frag, M.E.B. Mohamed, E.M. Fahim, Application of carbon sensors for potentiometric determination of copper(II) in water and biological fluids of Wilson disease patients. Studying the surface reaction using SEM, EDX, IR and DFT, Biosens. Bioelectron. 118 (2018) 122–128, https://doi.org/10.1016/j.bios.2018.07.024.
[16] E.Y. Frag, M.E. Mohamed, G.G. Mohamed, E.M. Fahim, Antibacterial, DFT and molecular docking studies of metformin complex as active material for the fabrication of copper (II) selective potentiometric sensor, Appl. Organomet. Chem. 33 (2019) e4986, https://doi.org/10.1002/aoc.4986.
[17] J. Fonseca, L. Meng, I. Imaz, D. Maspoch, Self-assembly of colloidal metal–organic framework (MOF) particles, Chem. Soc. Rev. 52 (2023) 2528–2543, https://doi.org/10.1039/D2CS00858K.
[18] V. Kavoosi, S.M. Masoudpanah, PVP-assisted MOF-derived $Fe_3O_4$/C powders for microwave absorption applications, Heliyon 11 (2025) e41202, https://doi.org/10.1016/j.heliyon.2024.e41202.
[19] C. McKinstry, E.J. Cussen, A.J. Fletcher, S.V. Patwardhan, J. Sefcik, Scalable continuous production of high quality HKUST-1 via conventional and microwave heating, Chem. Eng. J. 326 (2017) 570–577, https://doi.org/10.1016/j.cej.2017.05.169.
[20] A.M.V. Ganesh, S. Berchmans, Metal-organic framework-based electrode platforms in the assembly of biofuel cells and self-powered sensors, Chemelectrochem 9 (2022) e202200276, https://doi.org/10.1002/celc.202200276.
[21] H. Xiang, D. Baudouin, F. Vogel, Metal oxide nanoparticles embedded in porous carbon for sulfur absorption under hydrothermal conditions, Sci. Rep. 13 (2023) 9987, https://doi.org/10.1038/s41598-023-36395-8.
[22] J. Niu, X. Wang, Q. Wu, J. Li, D. Wang, F. Ran, Carbon/copper oxide electrode materials with high atomic utilization constructed by in-situ induced growth strategy of nano metal-organic frameworks, J. Colloid Interface Sci. 677 (2025) 68–78, https://doi.org/10.1016/j.jcis.2024.07.198.
[23] C. Zhao, H. Fu, P. He, Y. Bai, F. Chen, N. Shi, L. Mao, X. Yang, S. Xiong, X. An, Room-temperature sensing performance of CuO/$Cu_2O$ nanocomposites towards n-butanol, Sensor. Actuator. B Chem. 373 (2022) 132630, https://doi.org/10.1016/j.snb.2022.132630.
[24] R. Kaur, A. Kaur, A. Umar, W.A. Anderson, S.K. Kansal, Metal organic framework (MOF) porous octahedral nanocrystals of Cu-BTC: synthesis, properties and enhanced adsorption properties, Mater. Res. Bull. 109 (2019) 124–133, https://doi.org/10.1016/j.materresbull.2018.07.025.
[25] J.Y. Lee, J.H. Choi, Copper-based metal-organic framework for highly efficient adsorption of lead ions from aqueous solution, Mater. Res. Express 9 (2022) 095505, https://doi.org/10.1088/2053-1591/ac93ea.
[26] S. Xu, X. Guo, Z. Qiao, H. Huang, C. Zhong, Methyl-shield Cu-BTC with high water stability through one-step synthesis and in situ functionalization, Ind. Eng. Chem. Res. 59 (2020) 12451–12457, https://doi.org/10.1021/acs.iecr.0c02156.
[27] F. Israr, D.K. Kim, Y. Kim, S.J. Oh, K.C. Ng, W. Chun, Synthesis of porous Cu-BTC with ultrasonic treatment: effects of ultrasonic power and solvent condition, Ultrason. Sonochem. 29 (2016) 186–193, https://doi.org/10.1016/j.ultsonch.2015.08.023.
[28] A. Sahai, N. Goswami, S.D. Kaushik, S. Tripathi, Cu/$Cu_2O$/CuO nanoparticles: novel synthesis by exploding wire technique and extensive characterization, Appl. Surf. Sci. 390 (2016) 974–983, https://doi.org/10.1016/j.apsusc.2016.09.005.
[29] A. Ejsmont, T. Darvishzad, G. Słowik, P. Stelmachowski, J. Goscianska, Cobalt-based MOF-derived carbon electrocatalysts with tunable architecture for enhanced oxygen evolution reaction, J. Colloid Interface Sci. 653 (2024) 1326–1338, https://doi.org/10.1016/j.jcis.2023.09.172.
[30] A.S. Zoolfakar, R.A. Rani, A.J. Morfa, A.P. O'Mullane, K. Kalantar-zadeh, Nanostructured copper oxide semiconductors: a perspective on materials, synthesis methods and applications, J. Mater. Chem. C 2 (2014) 5247–5270, https://doi.org/10.1039/C4TC00345D.
[31] R.G. Kaldenhoven, J.M. Hill, in: J. Spivey, Y. Han (Eds.), Catalysis: Volume 30, vol. 30, The Royal Society of Chemistry, 2018, pp. 41–63, https://doi.org/10.1039/9781788013048-00041.
[32] A.J. Brandt, D.M. Shakya, K. Metavarayuth, E. Dolgopolova, L. Hensley, A.S. Duke, S. Farzandh, M. Stefik, N.B. Shustova, D.A. Chen, Growth of crystalline bimetallic metal–organic framework films via transmetalation, Langmuir 36 (2020) 9900–9908, https://doi.org/10.1021/acs.langmuir.0c01535.
[33] N. Rashid, F.A. Dar, M.A. Bhat, P.P. Ingole, Tailoring motif and channel terminating groups of conventional copper MOFs for their enhanced activity, selectivity, and stability toward the electroreduction of $CO_2$ to hydrocarbons, ACS Appl. Energy Mater. 6 (2023) 1378–1388, https://doi.org/10.1021/acsaem.2c03237.
[34] A. Jalal, Y. Zhao, A. Uzun, Pyrolysis temperature tunes the catalytic properties of CuBTC-Derived carbon-embedded copper catalysts for partial hydrogenation, Ind. Eng. Chem. Res. 61 (2022) 2068–2080, https://doi.org/10.1021/acs.iecr.1c04741.
[35] Q.T. Trinh, K. Bhola, P.N. Amaniampong, F. Jérôme, S.H. Mushrif, Synergistic application of XPS and DFT to investigate metal oxide surface catalysis, J. Phys. Chem. C 122 (2018) 22397–22406, https://doi.org/10.1021/acs.jpcc.8b05499.
[36] V.A. Edlabadkar, R.U. Soni, A.B.M.S. ud Doulah, S.Y. Owusu, S. Hackett, J. M. Bartels, N. Leventis, C. Sotiriou-Leventis, $CO_2$ uptake by microporous carbon aerogels derived from polybenzoxazine and analogous all-nitrogen polybenzodiazine aerogels, Chem. Mater. 36 (2024) 1172–1187, https://doi.org/10.1021/acs.chemmater.3c01717.
[37] J.A. Hondred, L. Medintz, J.C. Claussen, Enhanced electrochemical biosensor and supercapacitor with 3D porous architectured graphene via salt impregnated inkjet maskless lithography, Nanoscale Horiz 4 (2019) 735–746, https://doi.org/10.1039/C8NH00377G.
[38] P. Connor, J. Schuch, B. Kaiser, W. Jaegermann, The determination of electrochemical active surface area and specific capacity revisited for the system MnOx as an oxygen evolution catalyst, Z. Phys. Chem. 234 (2020) 979–994, https://doi.org/10.1515/zpch-2019-1514.
[39] R.S. Nicholson, I. Shain, Theory of stationary electrode polarography. Single scan and cyclic methods applied to reversible, irreversible, and kinetic systems, Anal. Chem. 36 (1964) 706–723, https://doi.org/10.1021/ac60210a007.
[40] E.P. Randviir, A cross examination of electron transfer rate constants for carbon screen-printed electrodes using electrochemical impedance spectroscopy and cyclic voltammetry, Electrochim. Acta 286 (2018) 179–186, https://doi.org/10.1016/j.electacta.2018.08.021.
[41] A.H. Shah, W. Zaid, A. Shah, U.A. Rana, H. Hussain, M.N. Ashiq, R. Qureshi, A. Badshah, M.A. Zia, H.B. Kraatz, pH dependent electrochemical characterization, computational studies and evaluation of thermodynamic, kinetic and analytical parameters of two phenazines, J. Electrochem. Soc. 162 (2014) H115, https://doi.org/10.1149/2.0481503jes.
[42] G.G. Graham, J. Punt, M. Arora, R.O. Day, M.P. Doogue, J. Duong, T.J. Furlong, J. R. Greenfield, L.C. Greenup, C.M. Kirkpatrick, J.E. Ray, P. Timmins, K.M. Williams, Clinical pharmacokinetics of metformin, Clin. Pharmacokinet. 50 (2011) 81–98, https://doi.org/10.2165/11534750-000000000-00000.
[43] P. Repiščák, S. Erhardt, G. Rena, M.J. Paterson, Biomolecular mode of action of metformin in relation to its copper binding properties, Biochemistry 53 (4) (2014) 787–795, https://doi.org/10.1021/bi401444n.
[44] M. Badea, M.N. Grecu, M.C. Chifiriuc, C. Bleotu, M. Popa, E.E. Iorgulescu, S. Avram, V. Uivarosi, A.C. Munteanu, D. Ghica, R. Olar, Insight on Ni(II) and Cu (II) complexes of biguanide derivatives developed as effective antimicrobial and antitumour agents, Appl. Organomet. Chem. 35 (2021) e6155, https://doi.org/10.1002/aoc.6155.
[45] S.M. Abu-el-Wafa, M.A. El-Ries, F.H. Ahmed, Formation of metformin complexes with some transition metal ions: their biological activity, Inorg. Chim. Acta. 136 (1987) 127–131, https://doi.org/10.1016/S0020-1693(00)81143-3.
[46] M.A.S. Sakr, M.A. Saad, O.H. Abd-Elkader, H. Abdelsalam, Q. Zhang, Promising sensors for pharmaceutical pollutant adsorption using Clar's goblet-based 2D membranes, Sci. Rep. 14 (2024) 889, https://doi.org/10.1038/s41598-023-50802-0.
[47] A. Zochedh, K. Chandran, M. Priya, A.B. Sultan, T. Kathiresan, Molecular simulation of naringin combined with experimental elucidation – pharmaceutical activity and molecular docking against breast cancer, J. Mol. Struct. 1285 (2023) 135403, https://doi.org/10.1016/j.molstruc.2023.135403.
[48] A.K. Gupta, N. Guh, S. Krishnan, P. Mathur, D.K. Rai, A three-dimensional Cu(II)-MOF with lewis acid−base dual functional sites for chemical fixation of $CO_2$ via cyclic carbonate synthesis, J. $CO_2$ Util. 39 (2020) 1011, https://doi.org/10.1016/j.jcou.2020.101173.
[49] R.C. Castro, D.S.M. Ribeiro, J.L.M. Santos, C. Nunes, S. Reis, R.N.M.J. Páscoa, Chemometric-assisted surface-enhanced Raman spectroscopy for metformin determination using gold nanoparticles as substrate, Spectrochim. Acta: Mol. Biomol. Spec. 287 (2023) 122118, https://doi.org/10.1016/j.saa.2022.122118.
[50] L.C. Chen, C.C. Chen, K.C. Liang, S.H. Chang, Z.L. Tseng, S.C. Yeh, C.T. Chen, W. T. Wu, C.G. Wu, Nano-structured CuO-$Cu_2O$ complex thin film for application in $CH_3NH_3PbI_3$ perovskite solar cells, nanoscal, Res. Let. 11 (2016) 402, https://doi.org/10.1186/s11671-016-1621-4.
[51] F. Marken, A. Neudeck, A.M. Bond, Cyclic voltammetry, in: F. Scholz (Ed.), Electroanalytical Methods, Springer, Berlin, Heidelberg, 2005, https://doi.org/10.1007/978-3-662-04757-6_4.
[52] J.G. Velasco, Determination of standard rate constants for electrochemical irreversible processes from linear sweep voltammograms, Electroanalysis 9 (1997) 880–882, https://doi.org/10.1002/elan.1140091116.
[53] A.K. Berekute, A.Y. Wang, K.Y. Lin, S. Siregar, K.P. Yu, A novel MOF-on-MOF-derived carbon-encapsulated $CeO_2$/Co/$Co_3O_4$ humidity-resistant heterojunction with abundant oxygen vacancies for efficient ozone removal, Environ. Res. 268 (2025) 120775, https://doi.org/10.1016/j.envres.2025.120775.
[54] M. Khan, A. Hameed, A. Samad, T. Mushiana, M.I. Abdullah, A. Akhtar, R. S. Ashraf, N. Zhang, B.G. Pollet, U. Schwingenschlögl, M. Ma, In situ grown oxygen-vacancy-rich copper oxide nanosheets on a copper foam electrode afford the selective oxidation of alcohols to value-added chemicals, Commun. Chem. 5 (2022) 109, https://doi.org/10.1038/s42004-022-00708-1.
[55] V.B. Patil, S.J. Malode, S.M. Tuwar, N.P. Shetti, Graphene sheet-based electrochemical sensor with cationic surfactant for sensitive detection of atorvastatin, Sens. Int. 3 (2022) 100198, https://doi.org/10.1016/j.sintl.2022.100198.
[56] W.B.S. Machini, I.P.G. Fernandes, A.M. Oliveira-Brett, Antidiabetic drug metformin oxidation and in situ interaction with dsDNA using a dsDNA-electrochemical biosensor, Electroanalysis 31 (2019) 1977, https://doi.org/10.1002/elan.201900162.
[57] A. Górska, B. Paczosa-Bator, J. Wyrwa, R. Piech, New electrochemical sensor of prolonged application for metformin determination based on hydrated ruthenium dioxide-carbon black-nafion modified glassy carbon electrode, Electroanalysis 32 (2020) 1875, https://doi.org/10.1002/elan.202060012.
[58] L. Wu, X. Lu, Y. Wu, C. Huang, C. Gu, Y. Tian, J. Ma, An electrochemical sensor based on synergistic enhancement effects between nitrogen-doped carbon nanotubes and copper ions for ultrasensitive determination of anti-diabetic metformin, Sci. Total Environ. 878 (2023) 163120, https://doi.org/10.1016/j.scitotenv.2023.163120.
[59] S. Dehdashtian, M.B. Gholivand, M. Shamsipur, Z. Karimi, A nano sized functionalized mesoporous silica modified carbon paste electrode as a novel,

simple, robust and selective anti-diabetic metformin sensor, Sensor. Actuator. B Chem. 221 (2015) 807–815, https://doi.org/10.1016/j.snb.2015.07.010.
[60] L.M.B. Jerez, U.M. García-Pérez, P. Zambrano-Robledo, J. Hernández-Moreira, Carbon paste electrode modified with $BiVO_4$ to sense metformin, Int. J. Electrochem. Sci. 9 (2014) 4643–4652, https://doi.org/10.1016/S1452-3981(23)08121-X.
[61] R. Mirzajani, S. Karimi, Preparation of γ-Fe2O3/hydroxyapatite/Cu(II) magnetic nanocomposite and its application for electrochemical detection of metformin in urine and pharmaceutical samples, Sensor. Actuator. B Chem. 270 (2018) 405, https://doi.org/10.1016/j.snb.2018.05.032.
[62] A. Nezhadali, Z. Khalili, Computer-aided study and multivariate optimization of nanomolar metformin hydrochloride analysis using molecularly imprinted polymer electrochemical sensor based on silver nanoparticles, J. Mater. Sci. Mater. Electron. 32 (2021) 27171–27183, https://doi.org/10.1007/s10854-021-07084-x.
[63] S. Zamani, Kh Ghanbari, S. Bonyadi, Electrochemical determination of metformin via a carbon paste electrode modified with an Ag NPs/Cu2O/CuO-decorated bacterial nanocellulose composite, Anal. Methods 15 (2023) 4606–4614, https://doi.org/10.1039/D3AY00703K.
[64] S. Hassasi, S.K. Hassaninejad-Darzi, A. Vahid, Production of copper-graphene nanocomposite as a voltammetric sensor for determination of anti-diabetic metformin using response surface methodology, Microchem. J. 172 (2022) 106877, https://doi.org/10.1016/j.microc.2021.106877.
[65] S. Dehdashtian, S. Wang, T.A. Murray, A comprehensive study of P-g-C3N4/MOF-199 composite for electrochemical sensing ofMetformin in pharmaceutical samples, Chemosensors 13 (2025) 82, https://doi.org/10.3390/chemosensors13030082.
[66] M. Hadi, H. Poorgholi, H. Mostaanzadeh, Determination of metformin at metal-organic framework (Cu-BTC) nanocrystals/multi-walled carbon nanotubes modified glassy carbon electrode, S. Afr. J. Chem. 69 (2016) 132–139. https://hdl.handle.net/10520/EJC190103.
[67] Y. Hao, H. Zhang, X. Yue, Z. Zhao, S. Zhao, A novel electrochemical sensor based on Cu(II) metal organic framework for the determination of metformin, Microchem. J. 191 (2023) 108849, https://doi.org/10.1016/j.microc.2023.108849.
[68] K. Danzer, Statistical evaluation of analytical results, in: Analytical Chemistry, Springer, Berlin, Heidelberg, 2007, https://doi.org/10.1007/978-3-540-35990-6_4.
[69] Y.J. Shih, S.K. Lin, Z.L. Wu, W.H. Chen, Cobalt and zinc imidazolate encapsulated in reduced graphene oxide and the derived nitrogen-enriched carbon frameworks (CoNC@rGO) for electrochemically sensing acetaminophen (APAP), Chem. Eng. J. 481 (2024) 148437, https://doi.org/10.1016/j.cej.2023.148437.